Selective Vapor-Phase Formation of Dimethylformamide via Oxidative Coupling of Methanol and Dimethylamine over Bimetallic Catalysts

Journal:	*Catalysis Science & Technology*
Manuscript ID	CY-ART-11-2023-001655.R1
Article Type:	Paper
Date Submitted by the Author:	23-Jan-2024
Complete List of Authors:	Minne, Alexander; The University of Alabama, Chemical and Biological Engineering Maxson, Tristan; The University of Alabama, Chemical and Biological Engineering Szilvasi, Tibor; The University of Alabama, Chemical and Biological Engineering Harris, James; The University of Alabama, Chemical and Biological Engineering

(to be submitted to Catalysis Science & Technology)

Selective Vapor-Phase Formation of Dimethylformamide via Oxidative Coupling of Methanol and Dimethylamine over Bimetallic Catalysts

Alexander P. Minne, Tristan Maxson, Tibor Szilvási, and James W. Harris*

Department of Chemical and Biological Engineering, The University of Alabama,
Tuscaloosa, AL, 35487

Abstract

The gas-phase oxidative coupling of methanol and dimethylamine (DMA) was investigated using bimetallic gold-based catalysts in a packed bed reactor. The selective coupling reaction yields dimethylformamide (DMF), a useful solvent for many chemical industries. Characterization of AgAu/SiO_2 and PdAu/SiO_2 catalysts reveal changes to the crystal and electronic structures of the metals indicative of predominantly alloyed nanoparticles. These alloy phases catalyze the oxidative coupling reaction of methanol and DMA to proceed with high selectivity towards DMF at low temperatures, whereas monometallic Ag or Pd catalysts are unselective and monometallic Au catalysts are unreactive. For PdAu/SiO_2 catalysts, increasing dilution of Pd in Au during synthesis results in increased gravimetric reaction rates (by 25 times) and rates per mol Pd (by 663 times), until both gravimetric and per Pd rates decrease as Pd is increasingly diluted in Au. These results suggest there is an optimum surface Pd ensemble size for oxidative coupling reactions, and that isolated Pd atoms are likely unreactive for this chemistry. DMF selectivity increases from monometallic Pd to alloyed Pd (from 45% to >75%), consistent with increasing isolation of oxygen rich domains capable of successive C-H cleavages leading to total oxidation products. Kinetic measurements show low reaction orders for the methanol (0-0.2), dimethylamine (0.1-0.5), and oxygen (0.1-0.2) reactants, alluding to high surface coverages. Co-feeding H_2O increased the rate of DMF formation, consistent with the increasingly basic surface adsorbates (i.e., hydroxyls) that are most reactive for kinetically relevant oxidative bond cleavages (e.g., C-H cleavage). Finally, DFT calculations and microkinetic modelling reveal surfaces of Pd(111) to be covered by surface oxygen and dehydrogenated DMA, the presence of which affect the reaction kinetics.

1. Introduction

Amide synthesis is estimated to be the most common reaction occurring in biological systems as well as pharmaceutical manufacturing, accounting for approximately 16% of all reactions in the manufacturing of modern medicine, and 25% of the drugs available on the market contain at least one amide bond.[1, 2] Similarly, dimethylformamide (DMF), a common solvent produced at $2.2*10^8$ kg yr^{-1} scale[3] is used as an industrial solvent due to its low volatile, highly aprotic nature, and wide liquid-phase range. Industries that use DMF include textiles, plastics, chemicals, automotive, pulp and paper, and electronics.[4] Currently, the one-step synthesis of DMF involves reacting N,N-dimethylamine (DMA) with carbon monoxide in a sodium methoxide-methanol mixture (0.5 -11 MPa, 323-473 K).[5] The residual sodium methoxide-methanol mixture must be neutralized with acid or water. CO and inert off-gases are released by decompression from the high pressure, unreacted DMA and methanol are then separated by distillation to achieve high purity DMF.[5] Alternatively, commercial grade methyl formate (96% purity) can be mixed with equimolar amounts of DMA (0.1-0.3 MPa and 333-373 K). Reacting methyl formate and DMA results in a mixture of DMF and methanol than can be separated by distillation.[5] Numerous patents have been licensed for synthesis of DMF. Many describe processes involving reacting DMA, CO and H_2 in a high-pressure batch process using homogenous catalysts,[6-9] some use continuous reactive distillation[10] and others use formamide or methyl formate as reactants to achieve the DMF product.[11-13] Because of the low price and green routes to methanol,[14-16] direct synthesis of DMF from methanol and DMA is touted as an improved synthesis technique that avoids the use of dangerous high pressure CO gas and expensive high purity methyl formate.

A continuous flow packed bed reactor, containing a transition metal heterogenous catalyst could offer a more economical and safer way to synthesize amides compared to liquid phase batch reactions requiring stoichiometric amounts of oxidants (such as Swern oxidation or Jones oxidation),[17-19] carbon monoxide or commercial grade methyl formate. Among potential transition metal catalysts are gold catalysts, historically thought to be inert,[20] but which have remarkable catalytic activities once absorbed oxygen atoms are present on the metallic surface.[21, 22] Studies of "nanoporous" catalysts prepared by dealloying of silver-gold alloys to form Au sponges have extensively documented the synthesis of methyl formate[23-26] and reported that of DMF[27, 28] by oxidative alcohol-alcohol coupling and oxidative alcohol-amine coupling in the liquid phase.

Oxidative alcohol self-coupling has been widely documented under both UHV conditions and industrially relevant conditions in liquid and gas phase.[23-28] The self-coupling of methanol produces methyl formate. The accepted mechanism for methanol self-coupling involves a surface oxygen assisted hydrogen elimination from a surface methoxy to create a formaldehyde intermediate, which is the limiting step in the reaction.[25] The electron deficient carbonyl carbon of the formaldehyde reacts with the electron-rich, nucleophilic oxygen of another surface methoxy species. A second hydrogen is removed from the carbonyl carbon by surface oxygen and methyl formate is produced. The competing reaction is the complete oxidation of the formaldehyde intermediate (Scheme 1).

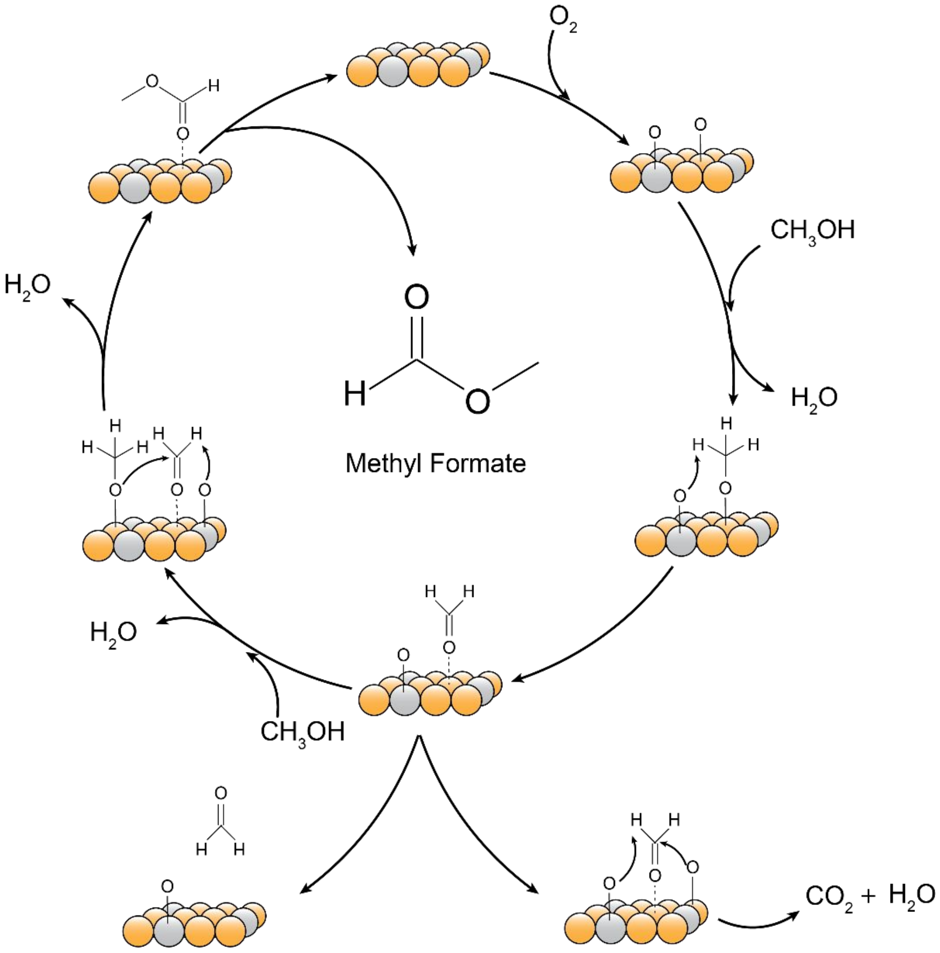

Scheme 1. Proposed reaction mechanism for the oxidative self-coupling of methanol on a dilute Ag in Au alloy surface.

Catalytic oxidative self-coupling of alcohols and cross-coupling of alcohols and amines on single crystals under UHV has previously been recorded.[29-32] In these studies, formaldehyde was successfully coupled with dimethylamine to yield DMF in near 100% selectivity on Ag(111) and Ag(110) with 0.1-0.5 ML of oxygen coverage, as well as pre-oxidized Au(111) (0.15 ML of oxygen). At higher oxygen coverages (1 ML) products such as NO_2, CO_2, H_2O, methyl isocyanate and methylformamide dominate and selectivity to DMF drops to 30%. Wichmann et al. reported liquid-phase methanol-dimethylamine coupling using nanoporous gold at moderate temperatures (298-333 K) and ambient pressure.[28] This provided concrete evidence that alcohols and amines can be coupled at industrially relevant conditions. The proposed mechanism for alcohol-amine coupling is similar to that of alcohol-alcohol coupling. The presence of DMA allows the possibility for aldehyde intermediates to react with the nucleophilic nitrogen of DMA instead of the carbonyl of formaldehyde, ultimately resulting in formation of dimethylformamide (Scheme 2). The rate determining step for DMF formation, similar to methanol-methanol coupling, is likely to be the Beta-H elimination that forms formaldehyde from adsorbed methoxy.[25, 27, 30, 33, 34] However, the hydrogen elimination step from the adsorbed hemiaminal intermediate ($(CH_3)_2NC(H_2)O_{ads}$) also could be rate-limiting.[32]

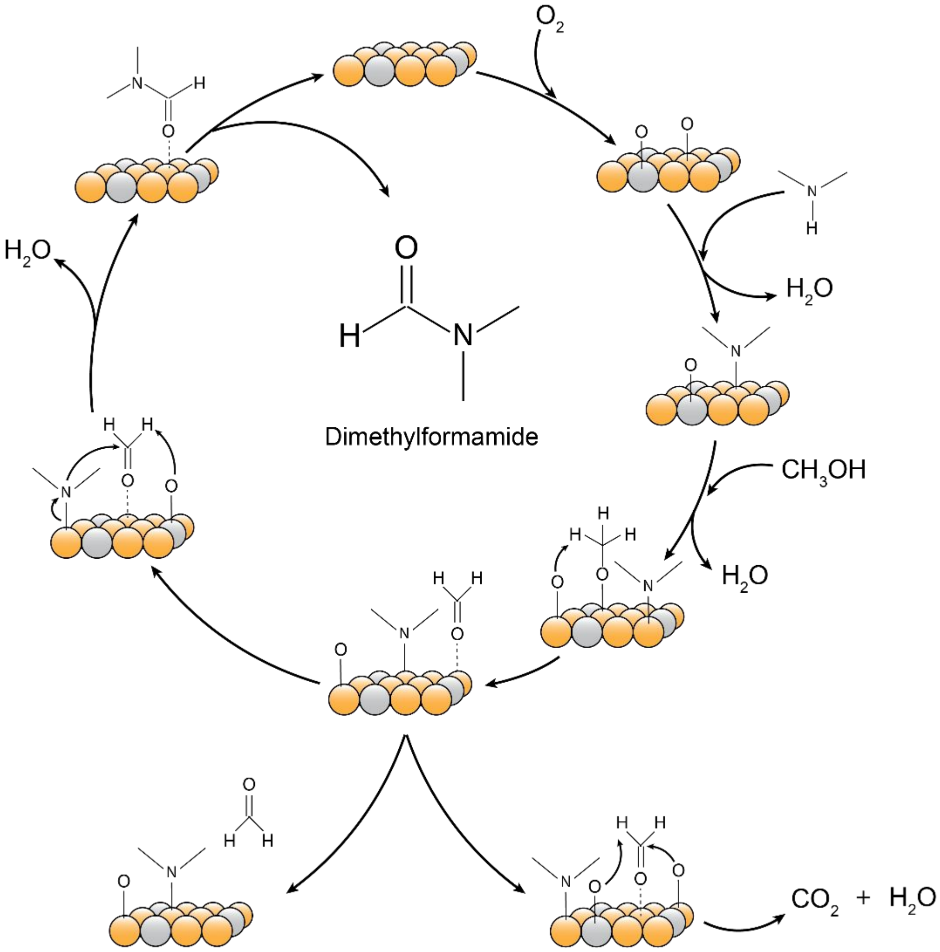

Scheme 2. Proposed reaction mechanism for the oxidative cross-coupling of methanol and dimethylamine on a dilute Ag in Au alloy surface.

Bulk Au is known to be inert for oxygen dissociation. O_2 adsorption is weak on Au surfaces, with DFT-calculated (Table S.1) adsorption enthalpies of 7.7 kJ mol^{-1} on Au(111)[35] and only slightly higher adsorption enthalpies on undercoordinated Au sites (14.5 and 16.4 kJ mol^{-1}, respectively, for Au(211)[36] and Au(321)[37]). The energy barriers for O_2 dissociation on Au surfaces (97, 108, and 132 kJ mol^{-1} over Au(111),[35] Au(211),[36] and Au(321),[37] respectively) are significantly higher than the O_2 absorption/desorption energies, even on step and kink sites in crystal structures where O_2 dissociation is not observed without high temperatures and pressures.[36] Table S.1 summarizes published values collected from literature.

O_2 dissociation by pure gold is often aided by contaminants,[38-41] basic pH conditions in condensed phases,[42] aqueous conditions,[43-45] and interactions of the Au with support surfaces.[46] When a dopant metal, such as Pd, is introduced to the Au surface in significant quantities (i.e., addition of one monolayer of Pd), the energy barrier for oxygen dissociation is reduced greatly, as shown in DFT studies performed on PdAu(111) surfaces.[47] 1-2 adjacent Pd atoms can dissociate O_2 with a relatively high energy barrier (116 kJ mol^{-1}) but an ensemble of six Pd atoms lowers the energy barrier (to 28.9 kJ mol^{-1}), lower than the desorption energy of O_2 (80.1 kJ mol^{-1}).[47] As a result, O_2 dissociation becomes energetically favorable to O_2 desorption on PdAu(111) surfaces containing contiguous ensembles of at least six Pd atoms.[47] Both Pd and Ag provide binding sites for oxygen dissociation in PdAu and AgAu alloys, as well as reactive metal oxides for hydrogen abstraction leading to aldehyde formation.[48]

Another possible mechanism for supplying oxygen adatoms to Au surfaces is by water-facilitated migration.[41-45, 49] In this mechanism, water adsorbs to the surface and dissociates to supply a surface hydrogen to an oxygen atom already present on the surface, typically originating from O_2 dissociation at the Au-support interface[46] or unintentional metal impurities[38, 39] and resulting in two mobile surface hydroxyl groups. Isotopically labelled ^{18}O water experiments over Au(110) demonstrated that recombination of hydroxyls to form water and an adsorbed oxygen adatom has a small energy barrier of 14.5 kJ mol^{-1}.[45] The potential relevance of the water-facilitated mechanism implies that, for example, trace water impurities cannot be ignored when observing changes in reaction rates as a result of reactant concentration changes. Kinetic data presented later also indicates the presence of water being highly influential in gaseous alcohol-amine coupling rate and selectivity.

Additionally, it is plausible that the phenomenon known as “hot atoms” is relevant for the bimetallic catalyst systems studied in this work. Reported by Klobas et al.,[50] this mode of O migration occurs via “hot atoms” that result from the kinetic energy generated from bond breaking that causes the previously bound atoms to gain translational energy. Translational energy then results in the adatoms moving away from their dissociation sites and across the metal surface. For example, in the case of O_2 dissociation on a Ag surface, the O^* surface species that exist after dissociation may not remain on the adjacent Ag atoms where the dissociation occurred. Instead, the atoms may translate to sites several atoms away. By translational motion, oxygen adatoms could migrate from a Ag ensemble to an adjacent Au surface, where they could participate in oxidation reactions. Hot atom translation can also result in the displacement of absorbed O_2 molecules and result in subsequent O_2.[50] At temperatures as low as 160 K on Ag(110) surfaces under UHV conditions, it was reported that the mean free path of hot oxygen adatoms is approximately 1.8 nm.[50] Therefore, it is possible for two oxygen atoms to be displaced for every dissociation event if they are within 0.58 nm, or 2 lattice units, of Ag(110).[50] It is unclear whether hot atoms is a viable mechanism for O* migration at conditions presented later in this work.

The structure of nanoporous gold or other metallic foams inherently results in low per metal reactivity, as many Au atoms will be located in the subsurface of the metal ligaments and inaccessible for catalysis. Additionally, the irregular pores of the sponge-like structure have the potential to introduce mass transfer limitations. To eliminate these drawbacks, supported nanoparticles could be used to maximize per metal atom reactivity, provide a high surface catalyst, and provide scalable synthesis for process intensification for oxidative alcohol-amine coupling. Supported catalysts for oxidative coupling have been reported for a variety of bimetallic combinations including PdAu,[51] PdCu,[52] and AgAu.[53]

In this work, synthesis methods and characterization of a series of catalysts including npAu and supported Pd, Au, Ag, AgAu and PdAu are demonstrated. The time-on-stream activity of the catalysts are examined with kinetic experiments in a gas-phase packed bed reactor. Data for variations in reactant partial pressure, temperature and product co-feeds is used to examine the effects on the selective formation of an amide bond in the vapor phase.

2. Experimental methods

2.1 Catalyst synthesis

Synthesis of nanoporous gold was completed following free-corrosion procedures similar to those reported previously.[24, 26, 54] White gold leaves (70% Ag, 30% Au, W&B Gold Leaf, LLC) were placed into a clean 120 cm^3 perfluoroalkoxy (PFA) jar (Savillex Corp.) and 70% nitric acid (Sigma Aldrich, 70%) was added dropwise to the jar. The solution was stirred between 1800 s and 48 hours to create samples with varied Ag content. The solids were centrifuged (5000 RPM) and washed three times (120 cm^3 g_{cat}^{-1} each wash) with millipore H_2O (18.2 MΩ) and then dried in a drying oven at 363 K in stagnant air for 24 hours.

Si-xerogel was prepared following the procedure from van Grieken et al.[55] 6.63 g of 0.1 M HCl(Sigma, 37% Reagent Grade) solution was stirred with 60.57 g of TEOS and 78.09 g of millipore H_2O (18.2 MΩ). The sample was stirred for 17 hours at ambient temperature. Then 1 M NH_4OH(Sigma, Reagent Grade) was added dropwise until the solution gelled. The gel was dried at 433 K for 24 hours. The solids were washed six times with millipore H_2O (18.2 MΩ), at which point the pH had stabilized at a value of 5.5. The solids were then dried at 433 K for 24 hours. Finally, the sample was calcined in flowing air ($1.67\ cm^3\ s^{-1}\ g^{-1}{}_{solid}$) at 823 K ($0.0167\ K\ s^{-1}$ ramp rate) for 10 hours.

Au/SiO_2 was synthesized by a urea deposition-precipitation method from Delannoy et al.[56] $HAuCl_4$ (VWR, <0.01% trace metals) was dissolved in 100 mL of millipore H_2O (18.2 MΩ) in a clean 120 cm^3 perfluoroalkoxy (PFA) jar (Savillex Corp.). Urea (Sigma,>99%) was added to the solution in a molar concentration 100 time greater than gold. Then, 1 g of heat-treated fumed silica (923 K for 12 hours) was stirred into the solution. The slurry was stirred for 16 hours at 353 K in a low light environment. Once cooled, the solids were recovered by centrifugation, and washed three times with millipore H_2O (18.2 MΩ) and then dried in vacuum at ambient temperature. The solids were calcined in a muffle furnace at 573 K for 4 hours. The process was repeated to make a 1wt% Au/SiO_2 catalyst for kinetic testing, and a 10wt% Au/SiO_2 catalyst for XRD and UV-Vis measurements.

Ag/SiO_2 was synthesized by incipient wetness impregnation. An aqueous solution of $AgNO_3$ (Sigma Aldrich, 99%) was made by dissolving 0.0765 g of $AgNO_3$ in 3 mL of millipore H_2O (18.2 MΩ). 1 g of heat-treated fumed silica (923 K for 12 hours) was placed in a clean 120 cm^3 perfluoroalkoxy (PFA) jar (Savillex Corp.) and the $AgNO_3$ solution was added dropwise to the fumed silica to effectively "wet" the silica, resulting in a gel-like slurry. The gel was allowed to slowly stir for 24 hours until the gel had dried. The solids were calcined in a muffle furnace at 723 K for 4 hours. The calcined solids were washed with millipore H_2O (18.2 MΩ) three times and recovered by centrifugation. Last, the solids were reduced in flowing H_2 (1.67 $cm^3\ s^{-1}$) at 723 K for 4 hours to obtain a 5wt% Ag/SiO_2 catalyst.

Pd/SiO_2 was prepared via incipient wetness impregnation. The metal precursor, $Pd(NO_3)_2 \cdot nH_2O$ (Sigma Aldrich, 99%), was dissolved in a volume of deionized water equal to the pore volume of the carrier in appropriate amounts to achieve the desired metal loading (1, 2, or 5 wt%) calculated on a metal basis. The precursor solution was added dropwise to the carrier, and the resulting materials were mixed at room temperature for 1 hour, then dried under vacuum (22.8 Torr) at 373 K for 12 hours, and finally calcined in air at 873 K for 5 hours using a heating rate of 0.083 K s^{-1}.

Silica supported AgAu nanoparticle catalysts were synthesized following the procedures of Liu et al.[57] SiO_2 was functionalized with 3-aminopropyltriethoxysilane (Sigma Aldrich, 99%) by ethanol reflux for 24 hours. The solids were washed with ethanol (VWR, 99.9%) five times (120 $cm^3\ g_{cat}^{-1}$ each wash) and dried before being dispersed in ambient temperature millipore H_2O (18.2 MΩ). A 1.65 wt% $HAuCl_4$ solution (VWR, <0.01% trace metals) was added while stirring at 500 RPM to introduce Au ions. After additional centrifuge filtration and five washes with millipore H_2O (18.2 MΩ), the solids were reduced by stirring in 20 cm^3 of 0.2 M $NaBH_4$ (Sigma Aldrich, >98.0%). The samples were washed with millipore H_2O (18.2 MΩ) five times to remove Cl^- ions before the Ag was added to solution. $AgNO_3$ (Sigma Aldrich, 99%) dissolved in minimal millipore H_2O was used as a precursor and was added to solution create a molar ratio of 1:15 Ag:Au. Again, the solids were recovered and washed with millipore H_2O (18.2 MΩ) and reduced with 20 cm^3 of 0.2 M $NaBH_4$ (Sigma Aldrich, >98.0%), then recovered and washed five more times. The solids were recovered and dried and then treated in flowing air (1.67 cm^3 g_{cat}^{-1} s^{-1}) at 723 K for 6 hours and then in flowing H_2 (Airgas, UHP, 1.67 cm^3 g_{cat}^{-1} s^{-1}) at 823 K for 1 hour to obtain the final AgAu/SiO_2. [58]

Silica supported PdAu nanoparticle catalysts were synthesized following the procedure from Liu et al.[59] $HAuCl_4 \cdot 3H_2O$ (VWR, 99.999%) was mixed with of polyvinylpyrrolidone (PVP, Sigma Aldrich, Lot# WXBD4555V) and ethylene glycol (VWR, >99%) in a 500 cm^3 round bottom flask. The solution was stirred, and the flask purged for one hour with N_2 (Airgas, UHP, 0.83 cm^3 s^{-1}) before $NaHCO_3$ (VWR, >99.7%) dissolved in minimal ethylene glycol was added by syringe injection through a septum sealing the neck of the round bottom flask. The solution was then heated in an oil bath to 363 K for 1800 s under N_2 protection until Au NPs were formed in solution. Once cooled to ambient temperature, the desired amount of $Pd(NO_3)_2 \cdot nH_2O$ (Sigma Aldrich, 99%) to reach target ratios of 1:1, 1:10, 1:50, 1:100 and 1:200 Pd:Au were mixed with 1 cm^3 ethylene glycol (VWR, >99%) and injected into the solution with a syringe. Next, 150 cm^3 of acetone (VWR, 99.5%) were added by syringe injection. The solution was centrifuged (10,000 RPM) to separate the solids from the acetone and ethylene glycol. The solids were washed with ethanol (VWR, 99.9%) and hexane (VWR, 99.5%) and dried in a vacuum oven (22.8 torr) at 298 K. The unsupported PdAu nanoparticles were redispersed in 100 cm^3 of stirred millipore H_2O (18.2 MΩ). 1 g of fumed silica (CABOT, Lot#4829189) was introduced into the aqueous solution of PdAu NPs and stirred overnight at ambient temperature. The solids were then separated by centrifugation and dried in a vacuum at ambient temperature for 24 hours.

Silica supported PdCu nanoparticle catalysts were synthesized following the procedures reported by Shan et al.[52] First, Cu/SiO_2 was synthesized under nitrogen protection (0.83 cm^3 s^{-1} flow) in a 500 cm^3 round bottom flask with a mixture of 0.3109 g of $Cu(NO_3)_2$ (Sigma, 99.99%)

and 0.2671 g of PVP in 28 cm^3 of an aqueous solution of 0.1 M ascorbic acid (VWR, 99%). Aqueous $NaBH_4$ (0.1 M) was added dropwise until the solution turned brown (~2 cm^3). Fumed silica was activated by treatment in flowing air at 923 K for 12 hours in a muffle furnace (0.0167 K s^{-1} ramp rate). The fumed silica was then suspended in H_2O to create a thick slurry and added drop-wise to the round bottom flask. The mixture was stirred under N_2 protection for 30 min and then centrifuged and washed with deionized water several times. The collected solids were dried in a vacuum oven (22.8 Torr) at ambient temperature for 12 hours. Next, the solids were treated in flowing air to 623 K for 4 hours (0.083 K s^{-1} ramp rate, 1.67 cm^3 g_{cat}^{-1} s^{-1}) and subsequently treated in a flow of hydrogen (Airgas, UHP, 99.999%, 1.67 cm^3 g_{cat}^{-1} s^{-1}) for 3 h at 623 K to obtain silica supported Cu NPs (Cu/SiO_2). Next, Pd atoms were deposited onto the Cu surfaces by galvanic replacement. The Cu/SiO_2 solids were suspended in 150 cm^3 water at ambient temperature and the required amounts of $Pd(NO_3)\cdot 6H_2O$ were added to reach target molar ratios of 1:1, 1:15, and 1:50 Pd:Cu. Then, the solution was stirred under N_2 protection (0.83 cm^3 s^{-1}) for 1 hour. The solids were filtered by centrifugation and washed with deionized water (40 cm^3 g_{cat}^{-1} per wash). The final solids were dried in vacuum at 333 K and treated in a flow of 10 kPa H_2, 90 kPa helium (1.67 cm^3 g_{cat}^{-1} s^{-1}) at 623 K for 1 hour (0.083 K s^{-1} ramp rate).

2.2 Catalyst characterization

Powder X-ray diffraction (XRD) patterns were collected using a Rigaku Miniflex XRD with a Cu X-ray source (kα = 1.542475 Å). XRD patterns were collected from 30^0 to 50^0 2-theta with a step size of 0.05° and scan rate of 0.0067° s^{-1}. Samples were pressed flush into the sample well of a zero-background holder.

Nitrogen physisorption isotherms were collected using a Micrometrics ASAP2020 Plus. Samples were pelleted using a pellet press (Carver) and die set (Specac) at 8000 psi, and ground in a mortar and pestle and sieved to 180-250 μm, before loading in a glass vacuum tube. Next, samples were treated at 623 K (1 K s^{-1} ramp rate) at ~1 μmHg for 9 hours. Then, the sample tubes were re-weighed, the degassed sample mass calculated, and the tube loaded to the analysis port for collection of N_2 adsorption isotherms (77 K).

Inductively coupled plasma optical emission spectroscopy (ICP-OES) (Agilent 5800) was used to determine the bulk elemental compositions of the various materials. Samples were digested in hydrofluoric acid (HF, 48%, VWR, 48%) overnight, followed by further digestion in aqua regia (HCl 37%, Sigma, HNO_3 70%, Sigma) overnight, then dilution in 2% nitric acid (prepared from 70% nitric acid, Sigma) in 125 cm^3 PTFE jars. *Note: HF and aqua regia are very hazardous, and appropriate safety considerations must be taken into account before use*. The instrument was calibrated before each use using standards prepared from 1000 ppm standards for Ag, Au, Cu, and Pd (Sigma, 1000 mg dm^{-3}).

UV-vis was collected using a Shimadzu 3600 Plus UV-VIS-NIR machine in a DRUV configuration with fumed silica as the material for background reflectance. Samples were lightly packed into the sample cup and the top surface was flattened with a clean glass slide. Data was collected between 200 and 800 nm at 0.1 nm intervals and an ultra-low scan rate (0.33 nm s^{-1}).

Scanning electron microscopy (SEM) images were collected with a Thermo Fisher Scientific Apreo SEM. A thin layer of powder sample was mounted with double-sided black carbon tape to hold the samples inside the vacuum chamber. High resolution transmission electron microscopy (HRTEM) images were collected on a FEI TECNAI F20 TEM. Samples were dispersed in methanol solvent (VWR, >99.9%), then sonicated to ensure high dispersion. One drop from the dispersed methanol-sample solutions was dripped onto Cu grids (EMS, 50 μm, 200 mesh) and the grids were left out to dry in ambient temperature and pressure for 24 hours before use.

Images were collected using 200k voltage and particle size distributions were determined from measurement of at least 70 particles per sample, using ImageJ software. TEM images were collected for both fresh and used catalysts to observe possible particle size changes as a result of extended exposure to reaction conditions.

2.3 Kinetic studies

Kinetic studies were conducted using as a continuous flow packed bed reactor as depicted in the process flow diagram shown in Figure S.1. Reactant partial pressures were varied while total pressure remained constant by varying the flowrate of He. The effluent stream of the reactor was analyzed using an Agilent 6890N/5975 GC/MS equipped with a TCD and FID. Columns used for chemical separation were an Alltech AT-Q (30 m x 0.53 mm) and Restek Shincarbon ST (2 m x 1 mm) in series to separate permanent gases preceding the TCD. An Agilent Porabond U column (25 m x 0.32 mm x 7 μm) was used for hydrocarbon separation before analysis on the FID and MS. A small amount of catalyst, typically less than 15 mg, was diluted with Si-xerogel two to three times the mass of catalyst and held between beds of quartz wool to form a packed-bed. This catalyst loading and use of a volumetric flow rate of ~1.67 cm^3 s^{-1} led to a sufficiently high space velocity to ensure the reactant conversions were always less than 10%. Catalysts were pretreated with procedures from Luneau et al.[60] Pretreatment procedure involved flowing 10 kPa O_2 in balance He at 50 cm^3 min^{-1}, then increasing the reactor temperature from ambient to 523 K at 0.033 K s^{-1} and holding for 1 hour. Then, while the reactor cooled down to 398 K, the reactor was switched to the reactant stream of 2.85 kPa methanol, 0.086 kPa DMA and 1.4 kPa O_2 in balance He with a CH_4 internal standard. All kinetic experiments began and ended at a standard condition which allowed for correction of the data for deactivation to calculate conversion, selectivity, and product rates. Deactivation corrections were made by fitting an exponential decay curve between the product rate at the standard condition at the beginning and end of the kinetic experiment. Then by using the following equation (eq. 1) where *r* designated product rate, *i* indicates each species, *o* represents measure rate before correction, *k* is the calculated decay constant, and *t* is time on stream.

$$r_{corrected} = \frac{r_{i,o}}{e^{kt}} \tag{1}$$

Conversion was calculated using Equation 2 where *f* is the molar flowrate of species *i*, and *b* is the flowrates measured in reactor bypass, and *s* is flowrate during time on stream.

$$X_i = \frac{f_{i,b} - f_{i,s}}{f_{i,b}} \tag{2}$$

Selectivity was calculated on a carbon basis. The number of carbons in the product was divided by the total number of carbons in carbon containing reactants on a flowrate basis. In Equation 3, *S* is carbon selectivity of product *i*, *n* is the number of carbons in the molecule and *f* is the flowrate. *a* is an index for summation across all reactants.

$$S_i = \frac{n_i * f_i}{\Sigma(n_a * f_a)} \tag{3}$$

2.4 Computational methods

Periodic Density Functional Theory (DFT) calculations are performed within the Vienna *ab initio* simulation package (VASP) version 6.3.1 and the Atomic Simulation Environment (ASE) version 3.23.0b1 with the Perdew-Burke-Ernzerhof (PBE) exchange functional and Grimme's D4 dispersion corrections.[61-69] A plane wave basis set a cutoff of 500 eV, VASP developer recommended PAW pseudopotentials (potpaw54), and a Gamma-centered Monkhorst-Pack k-point grid was used in all calculations. Gaussian smearing with a width of 0.1 eV is employed to allow for easier electronic convergence, except for gas phase calculations where a width of 0.02 eV is used to prevent unphysical partially occupied orbitals. All calculations are converged within

0.02 eV/Å maximum force threshold. Additional computational details can be found in the example input files added to the Supporting Information (SI). The second-order derivatives with respect to the position are calculated following the finite difference method of four displacements in each axis to ±0.01 Å with all surface atoms fixed. Vibrational modes smaller than 50 cm^{-1} are assumed to be numerical noise and are set to the value of 50 cm^{-1} following Truhlar's and Cramer's method.[70]

Bulk calculations were performed using the primitive cell and (15, 15, 15) k-point grids to optimize the cell lattice via the stress tensor. The calculated lattice constants are 4.103 Å and 3.906 Å for Au and Pd, respectively. Gas-phase calculations are performed with 16 Å of vacuum between molecules in all directions to avoid periodic interactions. The energy of gas phase diatomic oxygen ($E_{gas}^{O_2}$) is calculated by subtracting the experimental formation energy (5.116 eV) from twice the monotomic oxygen radical energy (E_{gas}^{O}) to avoid direct calculation of O_2 (which is known to be problematic in DFT) as seen in Equation 4.[71]

$$E_{gas}^{O_2} = \left(2 * E_{gas}^{O}\right) - 5.116 \text{ eV} \tag{4}$$

Surface models are derived from a (3×3) four-layer (111) surface. The bottom two layers are fixed in place and the remaining atoms are allowed to relax. Single-atom alloy (SAA) of Pd is simulated in the (3x3) cell by changing one surface atom formally creating a 1/9 monolayer surface layer coverage of Pd in Au(111) and is denoted as Pd/Au(111). 7 Å of vacuum are added on both sides of the slab, giving 14 Å of total vacuum. Surface calculations utilize a (5, 5, 1) k-point grid. A dipole correction is included in the vacuum direction to prevent spurious interactions between periodic images perpendicular to the surface.

Barriers are calculated using seven-image Nudged Elastic Band (NEB) calculations with a starting guess from the image-dependent pair potential.[72] NEB results are refined using the Dimer method as implemented in the VTST package for VASP.[73] Final Dimer calculations are converged to 0.01 eV/Å and transition states are confirmed via the presence of a single imaginary mode.

Gibbs free energies (G) are calculated as in Equation 5 at a temperature of 398 K as a representative reaction condition. The enthalpic contribution (pV), zero-point energy (ZPE), and entropy (S) are calculated according to the standard statistical mechanical equations including vibrational, rotational, and translation contributions via an in-house tool and added to the calculated DFT energy (E_{DFT}) in a standard thermodynamic treatment. All vibrations are treated as harmonic oscillators. Gas phase molecules additionally are considered as an ideal gas with translational and rotational modes identified and treated appropriately.

$$G = E_{DFT} + pV + ZPE - TS \tag{5}$$

The vibrational contribution of Gibbs free energy of binding (G_{bind}) is calculated as in Equation 6 by subtracting the Gibbs free energy of the clean surface ($G_{surface}$) and gas phase adsorbate ($G_{adsorbate}$) from the Gibbs free energy of the adsorbed molecule on the surface ($G_{surface+adsorbate}$). This chosen notation results in more negative binding energies when the adsorbate is bound stronger and positive binding energy correlates to weaker adsorption strength of an adsorbate.

$$G_{bind} = G_{surface + adsorbate} - G_{surface} - G_{adsorbate} \tag{6}$$

Microkinetic modeling simulations (MKM) were performed using Zacros 3.0.1 with no lateral interaction present to determine the surface coverage of intermediates at 398 K.[74] The molar fraction of inflow gas was taken to be 1% O_2, 2% MeOH, 0.013% DMA, and 0.007% H_2O to match with experimental conditions. The Pd(111) surface was modeled with a simple periodic 20 by 30 hexagonal lattice containing a total of 2400 sites. All adsorbates are considered to be monodentate in this work. It was assumed fast diffusion steps for all species in the beginning however, high surface coverages with close to zero empty surface sites make diffusion negligible in the simulation. All simulations have been performed until steady-state coverage and reaction rates have been observed.

3. Results and discussion

3.1 Structural characterization of catalysts

Catalysts were characterized by ICP-OES, UV-Vis, N_2 adsorption, XRD, SEM, and TEM (Table 1). N_2 adsorption demonstrates that the silica-supported materials generally have high surface areas, with those prepared from fumed silica having surface areas of averaging 160 m^2 g^{-1} while those prepared on silica gel had surface areas of ~550 m^2 g^{-1} (Figures S.2).

Table 1. Structural characterization data for the samples in this study.

Sample	Synthesis Method	Bulk Elemental composition[a]	V_{ads} (N_2, 77 K) (cm^3 g^{-1})[b]	S_{BET} (N_2, 77 K) (m^2 g^{-1})[b]	Dispersion (TEM)
npAu	Dealloying[24, 26, 54]	7 mol% Ag	0.0322	6.5 ± 1.8	-
Ag/SiO_2	I.W.I. [This Work]	-	-	-	-
Pd/SiO_2	I.W.I. [This Work]	-	0.1255	563 ± 9.3	15 ± 11
Au/SiO_2	DP Urea [56]	-	-	-	-
$AgAu/SiO_2$	Two-Step[57]	1:15	0.0488	182 ± 3.1	13 ± 6
$PdAu/SiO_2$	Two-Step[59]	1:2, 1:10, 1:53, 1:83, 1:148	0.0322	158 ± 3.2	15 ± 7
$PdCu/SiO_2$	Two-Step[75]	1:1 1:12	0.0375	148 ± 3.9	3.5 ± 1

[a] Bulk composition determined by inductively coupled plasma optical emission spectroscopy (ICP-OES).
[b] Surface area measurements determined by nitrogen physisorption at 77 K.

SEM images (Figures S.3-4) demonstrate that metal particles are dispersed across the surface of the SiO_2 supports. TEM images of at least 70 particles (and typically ~250 particles) were used to determine number average particle sizes. Example TEM images for $PdAu/SiO_2$, AgAu/SiO$_2$, and Pd/SiO$_2$ are shown in Figure 1, respectively. Additional TEM images are reported in the SI (Figures S.5-6). Average particle sizes from TEM range from 13-28 nm, demonstrating that the particles present on synthesized samples are sufficiently large, that (111) facets are expected to be prevalent, while undercoordinated Au sites in M-Au alloy particles will be minimal. Results from TEM images gathered on used samples show that the average particle size and distribution for all tested supported nanoparticle samples remained effectively unchanged after tens of hours at reaction conditions. Example images and size distribution graphs of used supported nanoparticle samples can be found in the SI (Section S.5, Figures S.7-9).

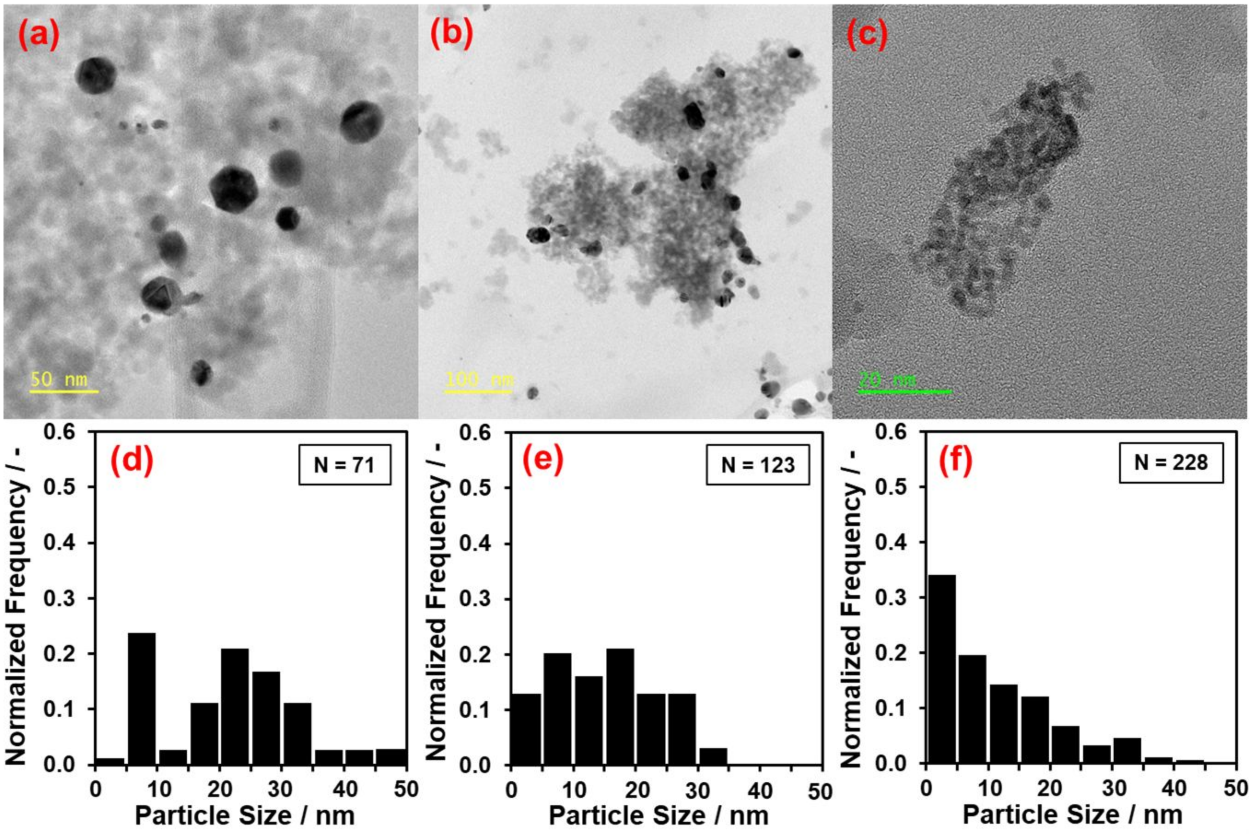

Figure 1. (a). TEM image of 1:10 PdAu/SiO$_2$. (b). TEM image of 1:15 AgAu/SiO$_2$. (c). TEM image of Pd/SiO$_2$. (d). Particle size distribution of 1:10 PdAu/SiO$_2$. (e). Particle size distribution of 1:15 AgAu/SiO$_2$. (f). Particle size distribution of Pd/SiO$_2$

Alloying of the Pd and Au can be seen in the (111) and (200) peak shifts between pure Au, pure Pd and 3 ratios of Pd and Au alloyed in the same nanoparticles (Figure S.10). Peak shifts are caused by lattice expansion and contraction due to Au and Pd having different atomic radii.[76] Low signal for the Pd/SiO_2 sample can be attributed to the relative low loading weight and small particle size of the sample, but the (111) peak at 40^0 is still visible as a low broad peak.

DRUV spectra were collected to assess the extent of alloying in the as-prepared catalyst samples (Figure S.11). In the pure Pd/SiO_2 and pure Au/SiO_2 samples, clear and characteristic localized surface plasmon resonance (LSPR) peaks are visible for the metals at 215 nm and 500 nm respectively.[77, 78] A distinct trend is seen in the Au LSPR peak as it diminishes with increasing Pd concentration. The trend in the Au LSPR peak alludes to the changing surface concentration of Au and Pd atoms in alloyed bimetallic particles.

3.2 Kinetics of methyl formate and dimethylformamide formation

The surface compositions of bimetallic nanoparticles are known to be responsive to process conditions during catalysis. A variety of pre-treatment protocols have been reported in order to reduce transients in surface composition and observed reactivity and selectivity for such materials for oxidation reactions. In this study, an *in situ* pretreatment protocol consisting of a mild oxidation treatment (heating to 473 K under 24 kPa O_2 and 98 kPa He) was used in an attempt to draw oxyphilic metals (i.e., Ag, Pd) to the surface of metal nanoparticles, based on guidance from Friend and co-workers.[24, 79] Next, the catalyst was exposed to the full reaction stream at 473 K, then cooled to reaction temperature (typically 398 K) and switched to the flowing reaction stream.

The results of the physical characterizations (Section 3.1) were used to perform empirical calculations regarding the relevance of heat and mass transfer limitations to the catalytic data reported in this manuscript. Using the GradientCheck tool developed by Hickman et al.,[80] and the surface areas and pore sizes determined from N_2 adsorption, it was determined that heat and mass transfer limitations were unlikely to impact the rates reported here. The output from GradientCheck along with the relevant parameters are reported in the Supplementary Information, Section S.8. With these pieces of information in hand, attempts to measure reaction rates for oxidative coupling reactions were made.

3.2.1 Kinetics Studies over nanoporous Au

Prior to exploring the potential for supported metal nanoparticle catalysts in catalyzing oxidative coupling between alcohols and amines, we first performed oxidative self-coupling of methanol to form methyl formate over nanoporous Au catalysts, as reported previously by several authors.[23, 24] Reactivity below 373 K was not observed, though formation of methyl formate with 78% selectivity and 1% methanol conversion was observed at 448 K (1.43 kPa O_2, 2.85 kPa CH_3OH, 1.43 kPa CH_4 balance He). The apparent activation energy for methyl formate formation was 43 ± 4 kJ mol^{-1} (428-458 K). A monometallic Ag/SiO2 catalyst was tested at these similar conditions to compare to the bimetallic nanoporous Au catalyst. At 448 K, Ag/SiO_2 was capable of oxidative self-coupling of methanol but with a selectivity of 45% and at a rate (per gram catalyst) that was an order of magnitude lower than that measured over nanoporous Au (Figure S.14). Judging these results as consistent (for a given methanol conversion) with previous reports, an attempt was made to perform oxidative coupling between alcohols and amines in the vapor phase.

Given concerns over the low vapor pressure of many amides, the smallest alcohol and the smallest dialkylamine (dimethylamine) were chosen as reactants. As expected based on the literature in liquid-phase[27, 81] and under ultra-high vacuum conditions,[82] nanoporous Au is capable of forming DMF in the vapor phase with high DMF selectivity (Figure 2). It is suspected that the bimetallic surface of nanoporous gold serves several catalytic purposes given the initial results of gas-phase methanol-dimethylamine oxidative coupling and previous literature. First, dilute quantities of Ag in the nanoporous gold allow for the dissociation of O_2 onto the surface and spillover onto nearby Au atoms.[38-41] Second, monoatomic oxygen on Au, provided by the dissociation of O_2 on Ag, allows for selective oxidation of absorbed methoxy species which produces a formaldehyde intermediate.[26, 30, 33] As a rate-limiting step in the oxidative self-coupling of methanol, it can be assumed that the same step has a relatively high energy barrier in this system.[23, 30, 33, 34] Third, the formaldehyde intermediate, produced by the first oxidation step, is selectively coupled to dimethylamine on the Au surface in a second oxidation step to create the C-N bond in the resulting dimethylformamide molecule. Xu et al. showed this formaldehyde-dimethylamine reaction was facile in UHV experiments, occurring with 100% selectivity and with an extremely low activation barrier on a pre-oxidized Au(111) surface.[31] The combination of these catalytic steps justifies the results of dimethylformamide product observed with a nanoporous Au catalyst in the Wichmann et al. liquid-phase oxidative coupling of methanol and dimethylamine studies,[28] as well as the gas-phase oxidative coupling of methanol and dimethylamine presented in this work.

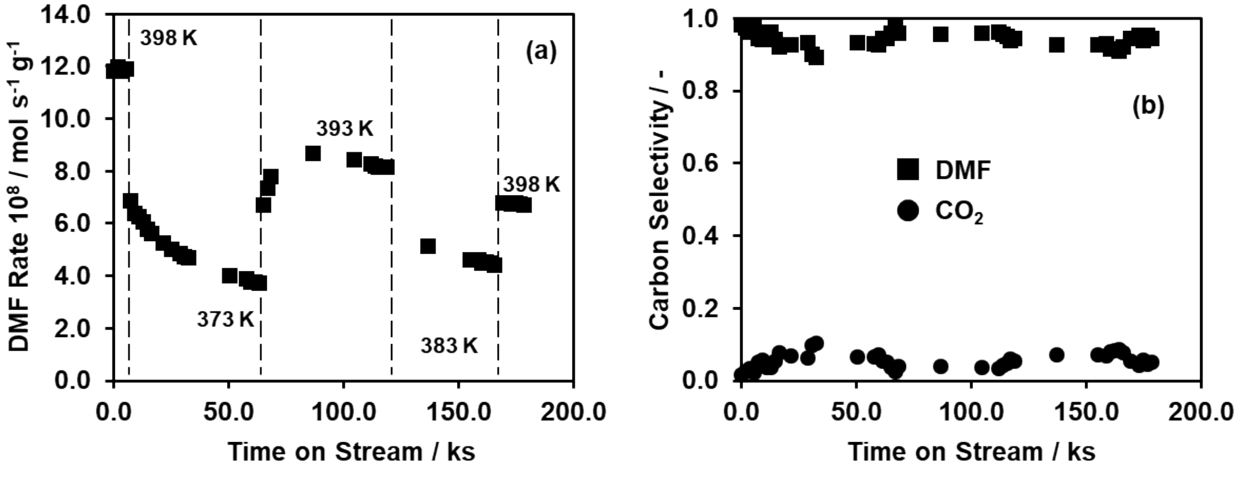

Figure 2. Rate during temperature variation and selectivity of gas-phase DMF formation on nanoporous gold.

After an initial break-in period to which steady DMF rates are observed as several hours, rates were measured at varied temperature (373-398 K) and O_2, methanol, and DMA pressures to determine the apparent reaction kinetics. Arrhenius plots (1.4 kPa O_2, 2.85 kPa methanol, 8.6 Pa DMA, 0.16 kPa CH_4, balance He; 373-448 K) are reported in Figure S.16 and the apparent activation energy is reported in Table 2. As shown in Figure S.17, the DMF formation rates were 0.09, 0.14, and 0.29 order in methanol, O_2, and DMA, respectively, over npAu. Apparent kinetics for CO_2 formation are reported in the S.I. (Figures S.20 and Table S.2).

Table 2. Summary of apparent activation energies and reaction orders of various samples tested in this study.

Catalyst	**CH_3OH self-coupling E_{app} / kJ mol^{-1}**	**DMA-CH_3OH coupling E_{app} / kJ mol^{-1}**	**DMA-methanol coupling reaction orders**			
			CH_3OH	**O_2**	**DMA**	**DMF**
npAu	43 ± 4.0	46 ± 6	0.09 ± 0.05	0.14 ± 0.06	0.29 ± 0.02	-
1:15 AgAu/SiO_2		75 ± 10	0.23 ± 0.02	0.18 ± 0.01	0.54 ± 0.05	-
Pd/SiO_2		46 ± 2	0.00 ± 0.02	0.17 ± 0.04	0.09 ± 0.04	-
1:10 PdAu/SiO_2		54 ± 3	0.02 ± 0.05	0.12 ± 0.03	0.15 ± 0.05	0

The apparent reaction order for each reactant was measured by varying the reactant concentration in a non-monotonic fashion while maintaining constant flowrate by varying He flow (Figure S.17). To negate long transients upon changes in reaction conditions (see Figure S.21) due to suspected restructuring of the catalyst, concentrations were varied within narrow ranges. Oxygen and DMA had the largest influence on the DMF production rate, with reaction orders of 0.14±0.06 and 0.29±0.02, respectively. The rate of DMF formation was not as significantly affected by methanol partial pressure (0.09±0.05 reaction order). The methanol reaction order during gas-phase methanol-DMA coupling result is distinct to the apparent methanol reaction order measured over nanoporous gold in the same system during gas-phase methanol-methanol coupling (0.9±0.06) (Figure S.15). Additionally, DMF was co-fed to probe for product inhibition (Figure S.22). It was determined from an on/off DMF co-feed experiment that DMF did not inhibit the DMF formation rate, even when DMF was fed in ~5× excess of what is produced experimentally. Based on the on/off experiment, it is determined that DMF does not inhibit reaction rates and it is not necessary to co-feed DMF in order to maintain a differential reactor.

Collectively, observed kinetic dependencies are consistent with a kinetically relevant step involving both a DMA-derived and a methanol-derived intermediate, and involvement of O_2-derived oxygen species. The low apparent reaction orders are indicative of high coverages of intermediates and/or the involvement of multiple surface sites in the kinetically relevant step(s). Reported next are the kinetics of DMF formation over a suite of silica-supported bimetallic catalysts.

3.2.2 Kinetic Studies over Silica-Supported Silver-Gold Catalysts

Silver-gold bimetallic nanoparticles were prepared via galvanic displacement following the procedures reported by Liu et al.[57, 58] The apparent activation energy for DMF formation over $AgAu/SiO_2$ was 88 ± 12 kJ mol^{-1}, significantly higher than that measured for methanol self-coupling and DMF formation over nanoporous Au (43 and 60 kJ mol^{-1}, respectively: Table 2). Apparent reaction orders for DMF formation were measured with respect to each of the reactants (Figure S.18 and Table 2). As expected for high O_2 partial pressures where oxygen was in excess, carbon selectivity towards the coupling product decreased in favor of combustion similar to results of gas-phase methanol coupling on nanoporous gold.[23] The low positive reaction orders were similar to those measured over npAu, though the methanol reaction order was more positive than that over npAu. As npAu and AgAu both catalyzed DMF formation, and given the relatively sparse literature related to supported AgAu nanoparticles, we next attempted to perform this reaction over other Au-based alloys, particularly PdAu, as PdAu[51, 83] and PdCu[75] catalysts have been reported to catalyze oxidative self-coupling of methanol previously, and the results reported thus far suggests catalysts that perform methanol self-coupling will also catalyze oxidative alcohol-amine coupling.

3.2.3 Kinetic Studies over Silica-Supported Palladium-Gold Catalysts

Similar to the AgAu catalysts, apparent activation energies and reaction orders for individual reactants were examined for supported PdAu catalysts. The apparent activation energy (Figure S.16 and Table 2) was slightly lower than that for AgAu/SiO_2. Apparent reaction orders (Figure 3 and Table 2) were comparable to those reported for AgAu/SiO_2. As was observed over npAu, the rate of DMF production on 1:10 PdAu/SiO_2 had little dependence on methanol and greater sensitivity to changes in DMA and O_2 concentration. The apparent reaction orders were 0.02±0.05 for methanol, 0.15±0.05 for DMA, and 0.12±0.03 for O_2. To determine if product inhibition by DMF was kinetically relevant, DMF was co-feed at various concentrations (Figure S.23). As was observed for npAu, no inhibition by DMF was observed for 1:10 PdAu/SiO_2 and we concluded it was not necessary to co-feed DMF in kinetic studies.

Co-feed experiments included the addition of H_2O feed to the system by helium flowing through a saturator at ambient temperature, resulting in a co-fed H_2O pressure of 0.0065 kPa. Water can react with O* already present on the Au surface and create two mobile hydroxyl groups. Hydroxyl groups can then recombine and leave a reactive oxygen species behind.[45] By this mechanism, we predict the excess water is creating surface hydroxyls that increase the quantity of reactive surface oxygen. A reaction order experiment involving the variation of oxygen concentration with a steady co-feed of water was then performed. The results showed an increase not only in DMF rate but as well as an increase in selectivity in excess oxygen conditions (Figure 3, grey triangles). Co-fed H_2O increased the DMF formation rate slightly (~0.15 order; see Figure 3 and Table 2), while also improving DMF selectivity under elevated O_2 pressures (i.e., above 5 kPa O_2). As shown in Figure 4, carbon selectivity towards the DMF coupling product is lost when O_2 kPa rises above 4 kPa. When H_2O is co-fed into the system, selectivity remains towards DMF until approximately 10 kPa of O_2.

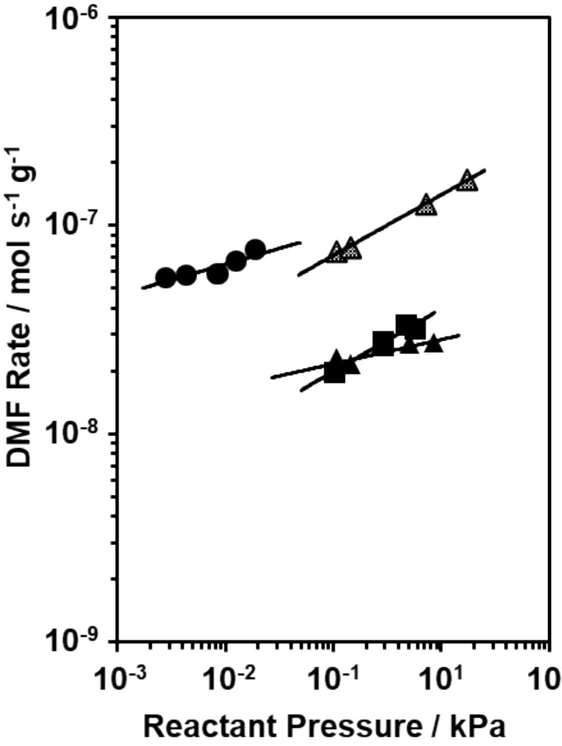

Figure 3. Reaction orders of DMA (circles), O_2 (triangles), methanol (squares) and O_2 reaction order with a H_2O co-feed (grey triangles). Reaction conditions: 141 kPa (1.00-5.70 kPa methanol, 1.10-8.56 kPa O_2, 0.014-0.156 kPa DMA, 0.0065 kPa H_2O (co-fed), 0.16 kPa CH_4, Balance He), 398 K, 1:10 PdAu/SiO_2 mass; 0.0054-0.0058 g diluted in Si-xerogel (approximately twice the catalyst mass) mg (GHSV: 197000 h^{-1}). Catalyst and Si-xerogel diluent sieved to 180μm-250 μm.

Two possible explanations for the observed increase in DMF selectivity are: first, hydroxyl groups from excess water recombine and leave behind atomic oxygen on Au where selective oxidation reactions occur[23, 42-45, 49] and second, hydroxyl groups occupy Pd-O sites that form in oxidant-rich conditions. Since palladium oxide catalyzes complete combustion of methanol in this system,[79] mobile hydroxyl groups formed from water occupy sites for complete oxidation, leading to the observed increase in DMF selectivity. A similar effect has been reported over Pd-O sites during methane oxidation catalysis, wherein excess water leads to surface hydroxyls blocking the Pd-O active sites.[84-87]

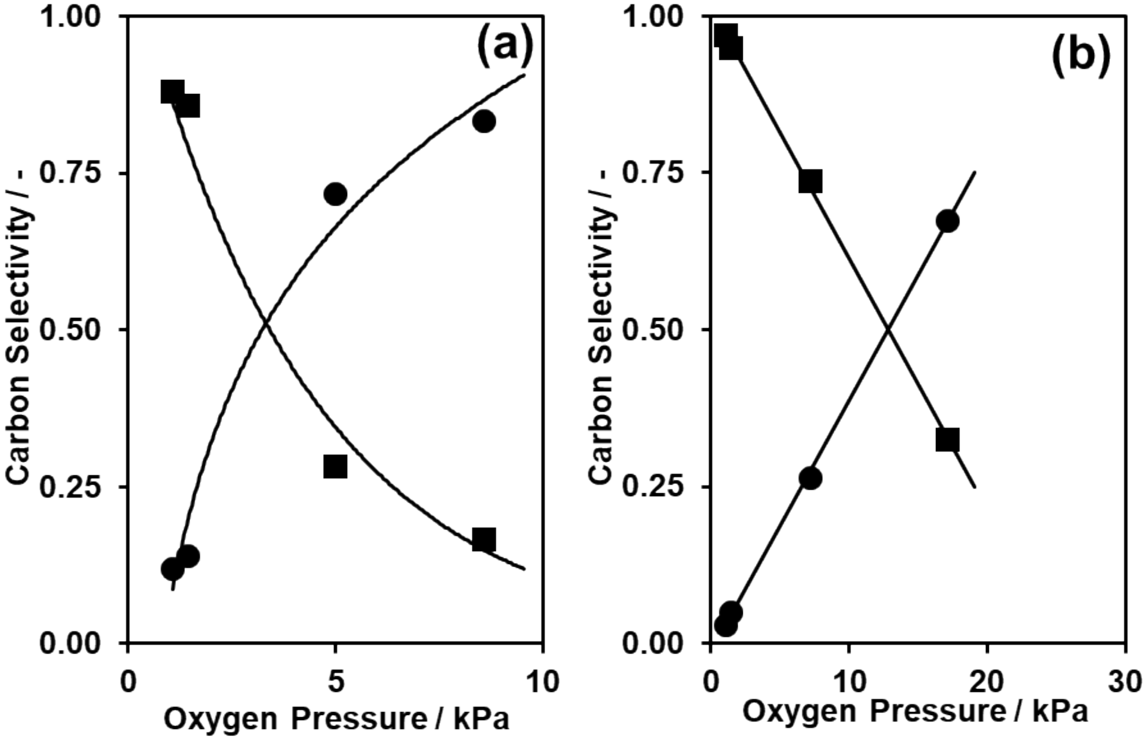

Figure 4. (a) Carbon selectivity of DMF (squares) and CO_2 (circles) during O_2 reaction order testing without H_2O co-fed. (b) Carbon selectivity of DMF (squares) and CO_2 (circles) during O_2 reaction order testing with additional 0.0065 kPa H_2O co-fed. Reaction conditions: 143 kPa (2.85 kPa methanol, 1.10-17.1 kPa O_2, 0.087 kPa DMA, 0.0065 kPa H_2O (co-fed), 0.16 kPa CH_4, Balance He), 398 K, 1:10 PdAu/SiO_2 mass; 0.0071 g diluted in Si-xerogel (approximately twice the catalyst mass). Catalyst and Si-xerogel diluent sieved to 180μm-250 μm.

Monometallic Pd/SiO_2 was also tested for comparison to PdAu/SiO_2. The DMF formation rate per gram catalyst was considerably much lower, while the DMF selectivity was also lower relative to PdAu (~50% vs. ~90 %). The DMF formation rate over Pd/SiO_2 was zero order in methanol pressure and the O_2 reaction order was 0.17, values that were similar to other bimetallic catalysts (Figure S.19 and Table 2). However, the apparent reaction order for DMF formation over Pd/SiO_2 with respect to DMA pressure was 0.09, lower than that observed over npAu (0.29), AgAu/SiO_2 (0.54), and within error of the slightly higher DMA reaction order over PdAu/SiO_2 (0.15). These results are consistent with prior results over monometallic Ag[88] and Pd[89] catalysts in methanol self-coupling reactions, in which nucleophilic surface oxygen adatoms and/or surface oxide domains predominantly catalyze successive oxidation reactions leading to a cascade from aldehydes to acids and ultimately formation of CO_2 and H_2O. We note however that at higher temperatures, Ag is used industrially for methanol oxidation to formaldehyde production,[88] as Ag suboxides are reduced under methanol-rich environments back to selective metallic Ag surfaces.

Decreasing the Pd:Au ratio results in a monotonic increase in rate per palladium and DMF selectivity, without decreases in the DMF formation rate per mass catalyst (Figure 5). The change in rate per Pd suggests increasing the isolation of Pd in Au avoids monometallic-like Pd domains that are unselective (on the basis of the monometallic Pd/SiO_2 results). However, monometallic Au/SiO_2 was inactive, suggesting there is an optimum Pd content in colloidal synthesized PdAu/SiO_2 to maximize DMF formation rate and selectivity. The optimum Pd:Au ratio likely exists somewhere between 1:53 Pd:Au and 1:83 Pd:Au, between which rates decrease while selectivity remains constant.

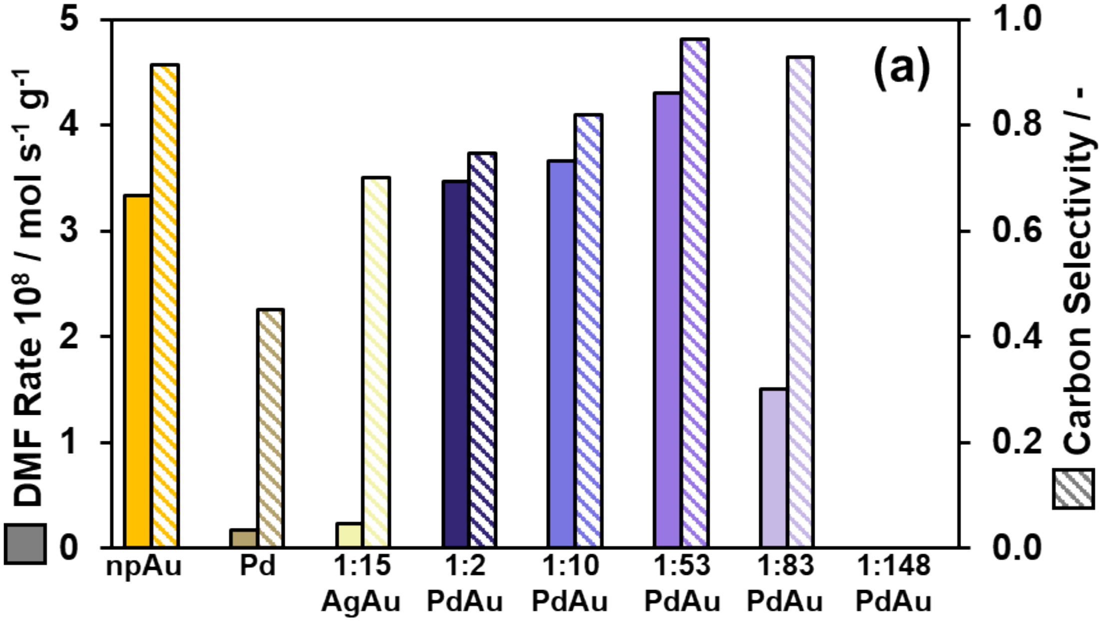

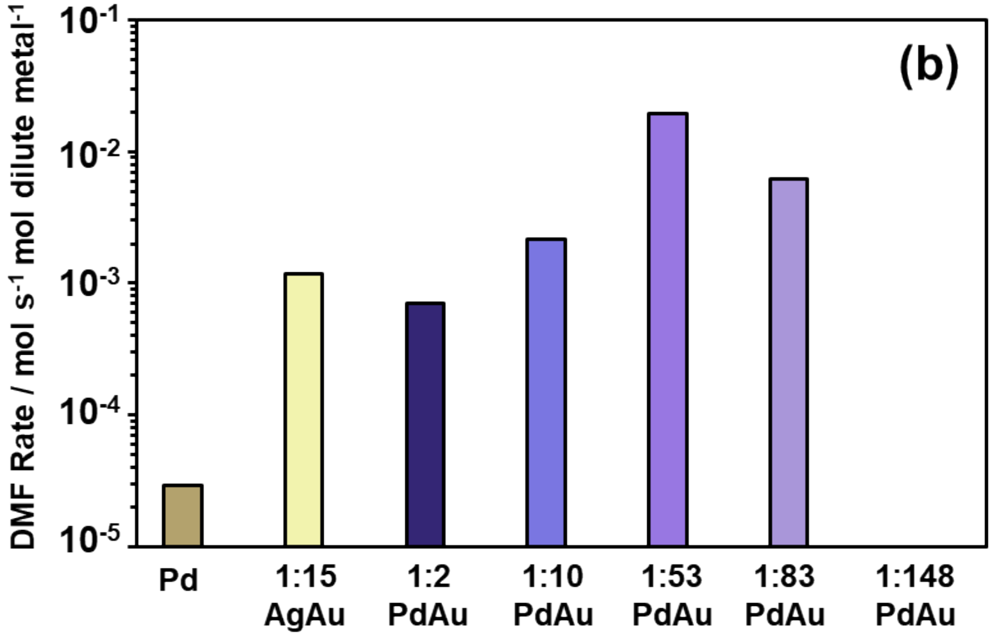

Figure 5. (a) Lefthand y-axis, solid bars: DMF rate per gram of catalyst; righthand y-axis, striped bars: carbon selectivity to DMF and (b) DMF rate per mol of Pd or Ag.

3.2.4 Computational Results

DFT calculations were carried out to gain insight into the reaction of DMA and MeOH coupling to form DMF on Pd(111), Au(111), and Pd/Au(111). The binding energies of plausible adsorbates on Pd(111), Au(111), and Pd/Au(111) and the reaction barriers among those adsorbates on Pd(111) and Au(111) were determined. Using calculated binding energies and reaction barriers, a microkinetic model for DMF formation was built to attempt to rationalize experimentally observed kinetics by trends in surface coverage.

Table 3 shows calculated Gibbs free binding energy of expected intermediates on various surfaces at 398 K during DMA/MeOH coupling to form DMF. DMA(-H) and DMF(H) represent dehydrogenated DMA and aldehyde-hydrogenated DMF, respectively. Pd/Au(111) refers to an isolated Pd single atom alloyed in the top surface of Au(111). While we note that samples with high Au:Pd ratios were less reactive than those with intermediate Au:Pd ratios, here an isolated Pd atom in Au is taken as a model to demonstrate likely differences in binding of adsorbates to PdAu alloy surfaces. Experimental PdAu alloy surfaces likely include configurations of dimers, trimers, tetramers, etc., for which computational studies are beyond the scope of the present work. For the single-atom alloy surface, adsorbate binding occurs at the single atom alloy site of Pd in all cases. The definition of Gibbs free binding energy and single atom alloy surface can be found in the computational methods section (§2.4). All structures are reported in the Supporting Information (SI).

Table 3. Calculated Gibbs free energy (eV) for binding of potential intermediates on various surfaces. DMA* and DMA(-H)* represent dimethylamine and its dehydrogenated form at nitrogen. DMF* and DMF(H)* represent dimethylformamide and its hydrogenated form at the aldehyde position. MeOH*, MeO*, and CH_2O* represent the species as methanol oxidizes to methoxy and finally to formaldehyde.

Species	**Au(111)**	**Pd/Au(111)**	**Pd(111)**
DMA*	-0.18	-0.31	-0.56
DMA(-H)*	-0.33	-0.45	-1.21
DMF*	-0.10	-0.11	-0.12
DMF(H)*	-0.57	-0.92	-1.60
MeOH*	0.34	0.22	0.18
MeO*	-0.39	-0.80	-1.30
CH_2O*	0.31	0.32	0.06
O*	-2.46	-2.88	-4.16
OH*	-1.33	-1.64	-2.15
H*	-1.63	-2.00	-2.45
H_2O*	1.06	0.91	1.05

Binding free energies at typical reaction conditions (398 K) show endergonic binding (>0 eV) of all stable gas phase species across all surfaces, except for DMA and DMF. DMA prefers to bind to all studied surfaces under reaction conditions. DMA binds the strongest with Pd(111) (-0.56 eV), however Pd/Au(111) (-0.31 eV) and Au(111) (-0.18 eV) are also exergonic. DMF binds weakly to Pd/Au(111) (-0.11 eV), Au(111) (-0.10 eV), and Pd(111) surfaces (-0.12 eV). O_2 is known to bind dissociatively to Pd(111)[90] and does not bind to Au(111)[91] thus binding of O_2 is not expected or shown in Table 3.

Table 4 shows reaction barriers at 398 K for considered reaction steps on Pd(111) and Au(111). The effect of co-adsorbed O/OH species are considered as they may assist with dehydrogenation steps and lower the reaction barrier.[49, 92] Species that are bound to the surface are indicated with * and adsorption/desorption steps are not shown.

Table 4. Reaction barriers at 398 K (in eV) for considered reaction steps on Pd(111) and Au(111). In dehydrogenation steps, the barrier in the presence of O* or OH* is also given to show changes due to co-adsorbates assisting with dehydrogenation.

Elementary Step	**Pd(111)**	**Au(111)**
$DMA^* \rightarrow DMA(\text{-}H)^* + H^*$	1.24	2.31
$DMA^* + O^* \rightarrow DMA(\text{-}H)^* + OH^*$	0.90	0.21
$DMA^* + OH^* \rightarrow DMA(\text{-}H)^* + H_2O^*$	0.59	0.43
$MeOH^* \rightarrow MeO^* + H^*$	0.36	0.33
$MeO^* \rightarrow CH_2O^* + H^*$	1.67	1.60
$MeO^* + O^* \rightarrow CH_2O^* + OH^*$	1.55	0.83
$MeO^* + OH^* \rightarrow CH_2O^* + H_2O^*$	1.20	0.54
$CH_2O^* + DMA(\text{-}H)^* \rightarrow DMF(H)^*$	0.06	0.11
$DMF(H)^* \rightarrow DMF^* + H^*$	0.87	0.95
$DMF(H)^* + O^* \rightarrow DMF^* + OH^*$	0.67	0.76
$DMF(H)^* + OH^* \rightarrow DMF^* + H_2O^*$	0.64	0.61
$H_2O^* + O^* \rightarrow OH^* + OH^*$	0.25	0.55
$OH^* + OH^* \rightarrow H_2O^* + O^*$	0.11	0.43

Barriers in the absence of O* or OH* are relatively high for dehydrogenation steps (> 1 eV) on both Pd(111) and Au(111) surfaces, except for the dehydrogenation of MeOH (< 0.4 eV) which should be facile on the studied surfaces even without a co-adsorbate present. The presence of O* or OH* decreases the reaction barriers for all dehydrogenation steps in the mechanism. On Pd(111), the barrier decreases from 1.67 eV with no co-adsorbate to 1.55 eV and 1.20 eV with O* and OH* co-adsorbates, respectively. On Au(111), the barrier decreases from 1.60 eV to 0.83 eV and 0.54 eV with O* and OH* present, respectively, showing a larger improvement compared with Pd(111). Calculated barriers indicate that O* or OH* co-adsorbates play in important role in accelerating the reaction if their surface coverage is signifgant. An almost barrierless reaction for CH_2O* and DMA(-H)* coupling on both Pd(111) and Au(111) is calculated, indicating that DMA(-H)* on all studied surfaces should immediately react with CH_2O* as it forms. As such, CH_2O* will be less likely to form side products (e.g., methyl formate) which is indeed not observed in any experiments where DMA is present.

Microkinetic modeling (MKM) simulations were performed to understand DMF formation on Pd(111). The MKM simulations indicate that the surface is entirely covered by O* and dehydrogenated DMA (DMA(-H)*) as shown in Figure 6. The high O* surface coverage (~0.9) indicates that there should essentially be no, or very low pressure dependence on O_2 for DMF production, which agrees well with experiments as seen in Figure 6. The surface coverage as a function of time is reported in Figure 6. Initially, methanol can adsorb to the surface and dehydrogenate to methoxy, but dehydrogenation to formaldehyde has the largest barrier among the required reaction steps of the reaction mechanism (Table 4). This is in agreement with the previous nanoporous Au studies in near ambient and UHV conditions that determine this step to be rate-limiting during oxidative methanol self-coupling.[23, 25-27] DMF(H)* decomposition back to CH_2O* and DMA(-H)* requires an empty site that is not present, which renders DMF(H)* formation practically irreversible. By manually decreasing the barrier of methanol dehydrogenation in our model, an increase in the reaction rate of DMF in the simulation is observed indicating that methoxy dehydrogenation is a rate determining step. The lowering of any other barriers in the model does not change the formation rate of DMF, indicating that the rate controlling step is specially the O-assisted methoxy dehydrogenation given the high O coverage of the surface and the reaction barrier for this step.

The results of MKM calculations on Pd(111) indicate very low surface coverage of methanol and methoxy. The surface coverage of methanol and methoxy agrees well with the kinetic data collected on a pure Pd/SiO_2 catalyst (Table 2, Figure S.19) where methanol was zero order, DMA was 0.09 order, and the apparent reaction order with respect to O_2 was 0.17. The MKM predicts an apparent methanol reaction order of 0.19 and an apparent DMA reaction order of 0.14. The MKM results also agree with experimental kinetic data that show an increase in the rate of DMF production with co-fed water, likely forming additional hydroxyls on the catalyst surface resulting in the lower OH barriers being accessible. The near barrierless reaction between dehydrogenated DMA and the formaldehyde intermediate is in line with absence of methyl formate (the methanol self-coupling product) detected despite the relatively low concentration of DMA compared to methanol in the reactant stream.

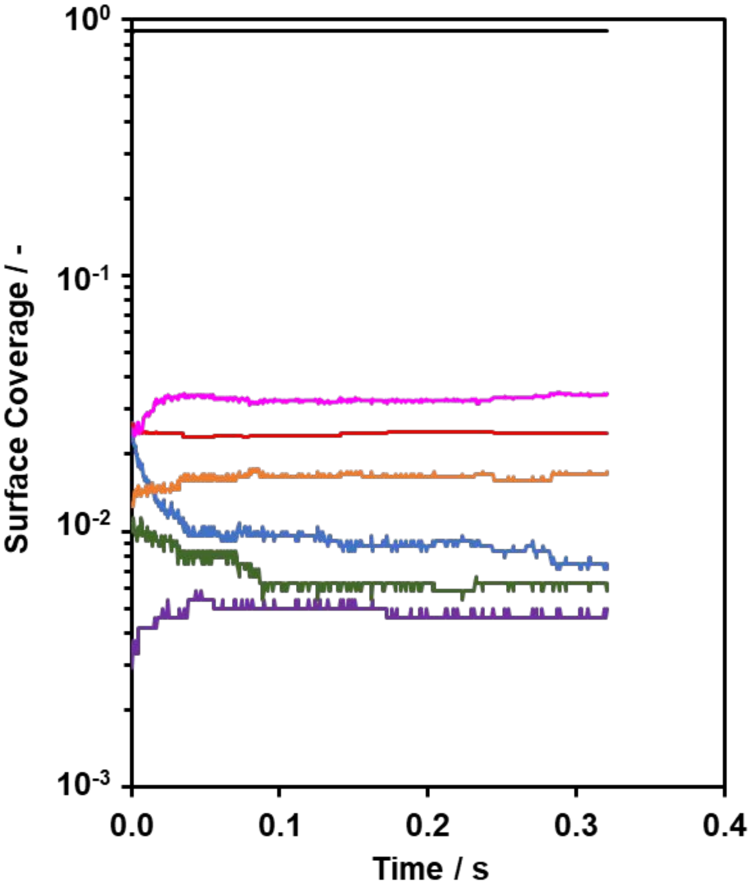

Figure 6. Microkinetic modeling of DMF formation on Pd(111). Coverages are reported for O* (black, solid), DMA(-H)* (black, dotted), OH* (red), CH_2O* (orange), DMA* (blue), CH_3O* (green) and H* (purple). Any surface species not plotted had coverages of zero. Converged calculations indicate a highly covered surface with O* and DMA(-H)* present.

The disagreements between computational modeling and experimental studies can be rationalized by a lack of lateral interactions and the plausibility that the (111) facet is likely not the sole location of kinetically relevant active sites. Surface coverages of ~0.9 ML of O* are unphysical and are an artifact of the lack of O*-O* interactions.[93] The coverage-consistent lateral interactions would presumably resolve the high O coverage issue and also affect the reaction barriers of the studied steps.[93, 94] The energy barrier of methoxy dehydrogenation is also calculated to be approximately three times higher on a Pd(111) surface compared with the apparent activation energy observed in the experimental kinetic measurements. Thus, it is hypothesized that active sites that are not located on the (111) surface must contribute significantly to the observed rate of reaction. The rate determining reaction barrier over sites not considered must also be lower than over the Pd(111) surface. Active sites with higher turnover frequencies would be concentrated on higher order facets, step edges, undercoordinated metals sites, and possibly metal-support interface sites. Further investigations into catalysts of systematically varied particle size, which would vary the ratio of the active site morphologies to the (111) facet surface area, should be conducted to better understand the nature of the active sites conducting the gas-phase oxidative coupling of methanol and dimethylamine. Computational studies investigating higher order facets, Pd surface ensembles of varied size and arrangement, and metal-support interface sites may be able provide calculated values for kinetically relevant steps that or more similar to the experimentally measured apparent activation energies.

3.3.1 Kinetics studies of other bimetallic alloys and monometallic metals supported on SiO_2

To better understand the role of Pd and Au in the PdAu alloy for the studied reaction, Au/SiO_2 and a PdCu/SiO_2 catalyst of a composition of 1:12 Pd:Cu was synthesized and tested at the same conditions subjected to AgAu, Pd, and PdAu alloy catalysts. At 398 K, DMF production was not quantifiable by FID with Au/SiO_2 or PdCu/SiO_2 catalysts. As expected Au/SiO_2 was not reactive in the system as Au alone lacks the ability to provide reaction surface oxygen by absorbed O_2 dissociation.[20] To produce a quantifiable amount of DMF with PdCu/SiO_2, the reaction temperature was increased to 428 K. At an elevated temperature of 428 K, a detectable amount of DMF was produced but the carbon selectivity was calculated at 0.3, which was lower than that observed on pure Pd/SiO_2 at 398 K. The increased temperature resulted in combustion of methanol that dominated over oxidative coupling and resulted in more CO_2 than DMF in the product stream. A comparative figure in the Supplementary Information (Figure S.24) shows the rates and selectivity of Pd/SiO_2, 1:10 PdAu/SiO_2, and 1:12 PdCu/SiO_2 at 398 K and 428 K. Additional Au and Cu based bimetallic alloy catalysts and monometallic counterparts (Pt, Cu, Ni, PtAu, PtCu, NiAu, NiCu) could be tested to probe whether selective the oxidative coupling of methanol and dimethylamine is unique to Au based catalysts doped with more reactive transition metals.

4 Conclusions

Gas-phase selective oxidative coupling of methanol and dimethylamine was observed at low temperatures (~398 K) over both nanoporous gold and silica-supported bimetallic nanoparticles catalysts in a gas-phase flow reactor. Instead of creating a C-O bond as in methanol-methanol oxidative coupling, the presence of a small amount of dimethylamine in the reactant stream entirely changed the selectivity of the oxidative coupling reaction mechanism towards C-N bond formation. Nanoparticle catalysts prepared by colloidal synthesis techniques resulted in particles averaging ~15 nm after thermal pretreatments. Further characterizations of bimetallic nanoparticle catalysts show geometric and electronic differences compared to monometallic supported nanoparticle catalysts consistent with formation of primarily alloyed particles.

A dilute palladium-in-gold nanoparticle catalyst was the most reactive bimetallic combination of those tested. At 398 K, DMF product can selectively be obtained under methanol rich conditions; an optimum in DMF formation rate and maximum carbon selectivity (~95%) was observed when the Pd:Au molar ratio was 1:53. As the Au:Pd ratio was increased further, the selectivity remained high, but the DMF formation rate decreased, indicating an apparent optimum in the ratio of surface Pd atoms to surface Au atoms for rate and selectivity with particles of this size (~15 nm). The apparent reaction orders of each catalyst tested are fractional and less than 0.5 for each reactant, consistent with a high surface coverage of reactants. The presence of water partial pressure in the reactant stream increases rate and selectivity, potentially due to increased surface hydroxyl concentrations. Previous literature and DFT calculations theorize that hydroxyls may help facilitate the dissociation of oxygen on large gold rich domains and also assist in the cleavage of C-H bonds.

Finally, DFT calculations on (111) facets of Pd, Au, and PdAu, and microkinetic modelling of Pd(111) confirm that the surface is highly covered in surface absorbates, the rate limiting step is the breaking of C-H bonds on absorbed methoxy surface species by a surface oxygen species, and the presence of a surface hydroxyl from excess moisture lowers the rate limiting step compared to a surface oxygen. The differences in energies at various calculated kinetically relevant steps and experimentally determined values indicate that a single crystal model does not capture the full distribution of true morphologies of the active sites contributing to DMF production rate.

Declaration of Competing Interest

The authors declare no competing financial interests.

Acknowledgements

The authors acknowledge Nohor "River" Samad for assistance with SEM-EDX images and nanoporous Au synthesis, Joshua Perch for synthesis of Pd/SiO_2, and assistance in collection of TEM images from The University of Alabama Analytical Research Center (AARC). The authors acknowledge financial support from the 2020-2021 UA ORED Small Grants Program, and financial support from the Alabama Water Institute and the Center for Water Quality that allowed for collection of ICP-OES data. A.P.M. and T.M. acknowledge funding from the U.S. Department of Education's GAANN Fellowship program. T.M. and T.S. would also like to thank the University of Alabama and the Office of Information Technology for providing high-performance computing resources and support that has contributed to these research results. This material is based upon work supported by the U.S. Department of Energy, Office of Science, Office of Advanced Scientific Computing Research, Department of Energy Computational Science Graduate Fellowship under Award Number(s) DE-SC0023112. This research used resources of the National Energy Research Scientific Computing Center (NERSC), a U.S. Department of Energy Office of Science User Facility located at Lawrence Berkeley National Laboratory, operated under Contract No. DE-AC02-05CH11231 using NERSC award BES-ERCAP0024218.

Appendix A. Supplementary material

Supplementary data to this article can be found online.

References

1. S. D. Roughley and A. M. Jordan, *Journal of Medicinal Chemistry*, 2011, **54**, 3451-3479.
2. P. W. Seavill and J. D. Wilden, *Green Chemistry*, 2020, **22**, 7737-7759.
3. H. Bipp and H. Kieczka, in *Ullmann's Encyclopedia of Industrial Chemistry*, John Wiley & Sons, Ltd, Weinheim, Germany, 2011, vol. 16, pp. 1-12.
4. N,N-Dimethylformamide, https://pubchem.ncbi.nlm.nih.gov/compound/N_N-Dimethylformamide).
5. H. Bipp and H. Kieczka, *Journal*, 2011.
6. *US Pat.,* US693111A, 1970.
7. *US Pat.,* US4098820A, 1978.
8. *US Pat.,* US3446842A, 1969.
9. *US Pat.,* US4558157A, 1985.
10. *US Pat.,* US2866822A, 1958.
11. *US Pat.,* US4853485A, 1989.
12. *US Pat.,* US6723877B1, 2004.
13. *US Pat.,* US3072725A, 1963.
14. E. G. Baker, L. K. Mudge and M. D. Brown, *Chemical Engineering Progress*, 1984, **80**, 43-46.
15. H. Nakagawa, T. Harada, T. Ichinose, K. Takeno, S. Matsumoto, M. Kobayashi and M. Sakai, *Japan Agricultural Research Quarterly: JARQ*, 2007, **41**, 173-180.
16. R. H. Williams, E. D. Larson, R. E. Katofsky and J. Chen, *Energy for Sustainable Development*, 1995, **1**, 18-34.
17. K. Omura and D. Swern, *Tetrahedron*, 1978, **34**, 1651-1660.
18. R. Chebolu, A. Bahuguna, R. Sharma, V. K. Mishra and P. C. Ravikumar, *Chemical Communications*, 2015, **51**, 15438-15441.
19. M. Zhao, J. Li, Z. Song, R. Desmond, D. M. Tschaen, E. J. J. Grabowski and P. J. Reider, *Tetrahedron Letters*, 1998, **39**, 5323-5326.
20. B. Hammer and J. K. Norskov, *Nature*, 1995, **376**, 238-240.
21. A. Wittstock, B. Neumann, A. Schaefer, K. Dumbuya, C. Kübel, M. M. Biener, V. Zielasek, H. P. Steinrück, J. M. Gottfried, J. Biener, A. Hamza and M. Bäumer, *The Journal of Physical Chemistry C*, 2009, **113**, 5593-5600.
22. B. Xu, R. J. Madix and C. M. Friend, *Acc. Chem. Res.*, 2013, **47**, 731-772.
23. A. Wittstock, V. Zielasek, J. Biener, C. M. Friend and M. Bäumer, *Science*, 2010, **327**, 319-322.
24. M. Personick, B. Zugic, B. Monika, B. Juergen, R. J. Madix and C. M. Friend, *ACS Catalysis*, 2015, **5**, 4237-4241.
25. A. Lackmann, C. Mahr, M. Schowalter, L. Fitzek, J. Weissmüller, A. Rosenauer and A. Wittstock, *Journal of Catalysis*, 2017, 99-106.
26. C. Reece, M. Leneau and R. J. Madix, *ACS Catalysis*, 2019, **9**, 4477-4487.
27. M. Personick, R. J. Madix and C. M. Friend, *ACS Catalysis*, 2017, **7**, 965-985.
28. A. Wichmann, Marcus Baumer, and Arne Wittstock, *ChemCatChem*, 2014, **7**, 70-74.

29. B. Xu, J. Haubrich, C. G. Freyschlag, R. J. Madix and C. M. Friend, *Chemical Science*, 2010, **1**, 310-314.
30. B. Xu, L. Xiaoying, J. Haubrich, R. J. Madix and C. M. Friend, *Angewandte Chemie*, 2009, **121**, 4270-4273.
31. B. Xu, L. Zhou, R. J. Madix and C. M. Friend, *A Journal of the German Chemical Society* 2010, **49**, 394-398.
32. L. Zhou, C. G. Freyschlag, B. Xu, C. M. Friend and R. J. Madix, *Chemical Communications*, 2010, **46**, 704-706.
33. B. Xu, J. Haubrich, T. A. Baker, E. Kaxiras and C. M. Friend, *The Journal of Physical Chemistry C*, 2011, **115**, 3703-3708.
34. B. Xu, R. J. Madix and C. M. Friend, *Journal of the American Chemical Society*, 2010, **132**, 16571-16580.
35. Y. Xu and M. Mavrikakis, *The Journal of Physical Chemistry B*, 2003, **107**, 9298-9307.
36. J. Kim, E. Samano and B. E. Koel, *Surface Science*, 2006, **600**, 4622-4632.
37. J. L. C. Fajín, M. N. D. S. Cordeiro and J. R. B. Gomes, *The Journal of Physical Chemistry C*, 2007, **111**, 17311-17321.
38. L. V. Moskaleva, S. Röhe, A. Wittstock, V. Zielasek, T. Klüner, K. M. Neyman and M. Bäumer, *Phys. Chem. Chem. Phys.*, 2011, **13**, 4529-4539.
39. M. W. Montemore, R. J. Madix and E. Kaxiras, *The Journal of Physical Chemistry C*, 2016, **120**, 16636-16640.
40. L. C. Wang, M. L. Personick, S. Karakalos, R. Fushimi, C. M. Friend and R. J. Madix, *Journal of Catalysis*, 2016, **344**, 778-783.
41. W. Dononelli, G. Tomaschun, T. Klüner and L. V. Moskaleva, *ACS Catalysis*, 2019, **9**, 5204-5216.
42. B. N. Zope, D. D. Hibbits, M. Neurock and R. J. Davis, *Science*, 2010, **330**, 74-78.
43. T. Fujitani, I. Nakamura and M. Haruta, *Catal Lett*, 2014, **144**, 1475-1486.
44. J. Saavedra, H. A. Doan, C. J. Pursell, L. C. Grabow and B. D. Chandler, *Science*, 2014, **345**, 1599-1602.
45. F. Xu, I. Fampiou, C. R. O'Connor, S. Karakalos, F. Hiebel, E. Kaxiras, R. J. Madix and C. M. Friend, *Phys. Chem. Chem. Phys.*, 2018, **20**, 2196-2204.
46. M. A. Montemore, M. A. van Spronsen, R. J. Madix and C. M. Friend, *Chemical Reviews*, 2018, **118**, 2816-2862.
47. W.-Y. Yu, L. Zhang, G. M. Mullen, G. Henkelman and C. B. Mullins, *The Journal of Physical Chemistry*, 2015, **119**, 11754-11762.
48. C.-R. Chang, B. Long, X.-F. Yang and J. Li, *The Journal of Physical Chemistry C*, 2015, **119**, 16072-16081.
49. L. Mastroianni, T. Weckman, K. Eränen, V. Russo, D. Y. Murzin, K. Honkala and T. Salmi, *Journal of Catalysis*, 2023, **425**, 233-244.
50. E. Klobas, .J, M. Schmid, C. M. Friend and R. J. Madix, *Surface Science*, 2014, **630**, 187-194.
51. A. Filie, T. Shirman, A. C. Foucher, E. A. Stach, M. Aizenburg, A. J., C. M. Friend and R. J. Madix, *Journal of Catalysis*, 2021, **404**, 943-953.
52. J. Shan, G. Giannakakis, J. Liu, S. Cao, M. Ouyang, M. Li, S. Lee and M. Flytzani-Stephanopoulos, *Topics in Catalysis*, 2020, **63**, 618-627.
53. Q. Z. Zhang, C.; Yang, G.; Sun, Y.; Wang, D.; Liu, J., *Catalysis Communications*, 2019, **129**, 105741.

54. B. N. Arne Wittstock, Andreas Schaefer, Karifala Dumbuya, Christian Kübel, Monika Biener, Volkmar Zielasek, Hans-Peter Steinrück, J. Mickael Gottfried, Jürgen Beiner, Alex Hamza, Marcus Bäumer, *The Journal of Physical Chemistry C*, 2009, **113**, 5593-5600.
55. R. van Grieken, C. Martos, M. Sánchez-Sánchez, D. P. Serrano, J. A. Melero, J. Iglesias and A. G. Cubero, *Microporous and Mesoporous Materials*, 2009, **119**, 176-185.
56. L. Delannoy, N. El Hassan, A. Musi, N. N. Le To, J. M. Krafft and C. Louis, *J. Phys. Chem. B*, 2006, **110**, 22471-22478.
57. X. Liu, A. Wang, X. Yang, T. Zhang, C.-Y. Mou, D.-S. Su and J. Li, *Chemistry of Materials*, 2009, **21**, 410-418.
58. X. Liu, A. Wang, L. Li, T. Zhang, C.-Y. Mou and J.-F. Lee, *Progress in Natural Science: Materials International*, 2013, **23**, 317–325.
59. J. Liu, J. Shan, F. R. Lucci, S. Cao, C. Sykes and M. Flytzani-Stephanopoulo, *Catal. Sci. Technol.*, 2017, **7**, 4276-4284.
60. M. Luneau, E. Guan, W. Chen, A. C. Foucher, N. Marcella, T. Shirman, D. M. A. Berbart, J. Aizenburg, M. Aizenburg, E. A. Stach, R. J. Madix, A. I. Frenkel and C. M. Friend, *Communications Chemistry*, 2020, **3**, 1-9.
61. G. Kresse and J. Furthmüller, *Physical Review B*, 1996, **54**, 11169-11186.
62. G. Kresse and J. Furthmüller, *Computational Materials Science*, 1996, **6**, 15-50.
63. G. Kresse and J. Hafner, *Physical Review B*, 1993, **47**, 558-561.
64. G. Kresse and D. Joubert, *Physical Review B*, 1999, **59**, 1758-1775.
65. J. P. Perdew, K. Burke and M. Ernzerhof, *Physical Review Letters*, 1996, **77**, 3865-3868.
66. A. Hjorth Larsen, J. Jørgen Mortensen, J. Blomqvist, I. E. Castelli, R. Christensen, M. Dułak, J. Friis, M. N. Groves, B. Hammer, C. Hargus, E. D. Hermes, P. C. Jennings, P. Bjerre Jensen, J. Kermode, J. R. Kitchin, E. Leonhard Kolsbjerg, J. Kubal, K. Kaasbjerg, S. Lysgaard, J. Bergmann Maronsson, T. Maxson, T. Olsen, L. Pastewka, A. Peterson, C. Rostgaard, J. Schiøtz, O. Schütt, M. Strange, K. S. Thygesen, T. Vegge, L. Vilhelmsen, M. Walter, Z. Zeng and K. W. Jacobsen, *Journal of Physics: Condensed Matter*, 2017, **29**, 273002.
67. E. Caldeweyher, C. Bannwarth and S. Grimme, *The Journal of Chemical Physics*, 2017, **147**, 034112.
68. E. Caldeweyher, S. Ehlert, A. Hansen, H. Neugebauer, S. Spicher, C. Bannwarth and S. Grimme, *The Journal of Chemical Physics*, 2019, **150**, 154122.
69. E. Caldeweyher, J.-M. Mewes, S. Ehlert and S. Grimme, *Physical Chemistry Chemical Physics*, 2020, **22**, 8499-8512.
70. R. F. Ribeiro, A. V. Marenich, C. J. Cramer and D. G. Truhlar, *The Journal of Physical Chemistry B*, 2011, **115**, 14556-14562.
71. E. Sargeant, F. Illas, P. Rodríguez and F. Calle-Vallejo, *Journal of Electroanalytical Chemistry*, 2021, **896**, 115178.
72. G. Henkelman, B. P. Uberuaga and H. Jónsson, *The Journal of Chemical Physics*, 2000, **113**, 9901-9904.
73. G. Henkelman and H. Jónsson, *The Journal of Chemical Physics*, 1999, **111**, 7010-7022.
74. J. Nielsen, M. d'Avezac, J. Hetherington and M. Stamatakis, *The Journal of Chemical Physics*, 2013, **139**, 224706.
75. J. Shan, G. Giannakakis, J. Liu, S. Cao, M. Ouyang, M. Li, S. Lee and M. Flytzani-Stephanopoulos, *Topics in Catalysis*, 2020, **63**, 618-627.

76. T. Naoki, Y. Hu, S. Yiukihide, B. Corain, G. Schmid and N. Toshima, in *Metal Nanoclusters in Catalysis and Materials Science*, Elsevier, Amsterdam, 2008, ch. 3, pp. 49-75.
77. W. Haiss, N. T. K. Thanh, J. Aveyard and D. G. Fernig, *Anal. Chem.*, 2007, **79**, 4215-4221.
78. M. Wen, S. Takakura, K. Fuku, K. Mori and H. Yamashita, *Catalysis Today*, 2015, **242**, 381-385.
79. B. Zugic, L. Wang, C. Heine, D. N. Zakharov, B. A. J. Lechner, E. A. Stach, J. Biener, M. Salmeron, R. J. Madix and C. M. Friend, *Nature Materials*, 2017, **16**, 558-564.
80. D. A. Hickman, J. C. Degenstein and F. H. Ribeiro, *Current Opinion in Chemical Engineering*, 2016, **13**, 1-9.
81. S. Tanaka, T. Minato, E. Ito, M. Hara, Y. Kim, Y. Yamamoto and N. Asao, *Chemistry – A European Journal*, 2013, **19**, 11832-11836.
82. B. Xu, R. J. Madix and C. M. Friend, *Accounts of Chemical Research*, 2014, **47**, 761-772.
83. J.-b. Wu, R.-p. Shi, Z.-f. Qin, H. Liu, Z.-k. Li, H.-q. Zhu, Y.-x. Zhao and J.-g. Wang, *Journal of Fuel Chemistry and Technology*, 2019, **47**, 780-790.
84. A. Boucly, L. Artiglia, M. Roger, M. Zabilskiy, A. Beck, D. Ferri and J. A. van Bokhoven, *Applied Surface Science*, 2022, **606**.
85. C. F. Cullis, T. G. Nevell and D. L. Trimm, *Journal of the Chemical Society, Faraday Transactions 1: Physical Chemistry in Condensed Phases*, 1972, **68**, 1406-1412.
86. R. Burch, F. J. Urbano and P. K. Loader, *Applied Catalysis A: General*, 1995, **123**, 173-184.
87. W. R. Schwartz, D. Ciuparu and L. D. Pfefferke, *The Journal of Physical Chemistry C*, 2012, **116**, 8587-8593.
88. M. Karatok, M. G. Sensoy, E. I. Vovk, H. Ustunel, D. Toffoli and E. Ozensoy, *ACS Catalysis*, 2021, **11**, 6200-6209.
89. R. Wojcieszak, A. Karelovic, E. M. Gaigneaux and P. Ruiz, *Catal. Sci. Technol.*, 2014, **4**, 3298-3305.
90. T. Szilvási, H. Yu, J. I. Gold, N. Bao, T. J. Wolter, R. J. Twieg, N. L. Abbott and M. Mavrikakis, *Materials Horizons*, 2021, **8**, 2050-2056.
91. H. Yu, T. Szilvási, K. Wang, J. I. Gold, N. Bao, R. J. Twieg, M. Mavrikakis and N. L. Abbott, *Journal of the American Chemical Society*, 2019, **141**, 16003-16013.
92. H. Schubert, U. Tegtmeyer and R. Schlögl, *Catalysis Letters*, 1994, **28**, 383-395.
93. D. H. Parker and B. E. Koel, *Journal of Vacuum Science & Technology A*, 1990, **8**, 2585-2590.
94. S. Bhandari, S. Rangarajan and M. Mavrikakis, *Accounts of Chemical Research*, 2020, **53**, 1893-1904.